

A Large-Eddy Simulation Study of Scalar Dissimilarity in the Convective Atmospheric Boundary Layer

DIANA M. CANCELLI

Graduate Program in Numerical Methods in Engineering (PPGMNE), Federal University of Paraná, Curitiba, Brazil

MARCELO CHAMECKI

Department of Meteorology, The Pennsylvania State University, University Park, Pennsylvania

NELSON L. DIAS

Department of Environmental Engineering, Federal University of Paraná, Curitiba, Brazil

(Manuscript received 11 April 2013, in final form 14 September 2013)

ABSTRACT

A numerical study of the effect of entrainment fluxes at the top of the atmospheric boundary layer (ABL) on dissimilarity between scalars within the mixed and surface layers is conducted. Simulation results clearly show that entrainment fluxes of opposite sign cause decorrelation between the scalars throughout the entire ABL. In the upper part of the mixed layer, this decorrelation is caused by changes in the covariance between the scalars and the scalar variance as well, and is distributed over the entire range of scales resolved in the simulation. Near the surface, the reduction in correlation coefficient originates from an increasing scalar variance, which is present exclusively in the large scales. These effects are noticeable on time scales of about 24 min or longer, and could be interpreted as nonstationarity for the typical 30-min periods used in surface-layer data processing. In addition, it is shown that, for the conditions studied here, the scalar correlation coefficient within the surface layer scales with the measurement height normalized by the ABL depth and not by the Obukhov length.

1. Introduction

Similarity between temperature and specific humidity is key to many methods used to estimate evaporation (e.g., Wesely 1988; Asanuma et al. 2005; Cancelli et al. 2012) and to retrieve estimates of surface fluxes from scintillometers (Li et al. 2012). Similarity assumptions can also be used to model fluxes of other gases, including pollutants and greenhouse gases such as CO₂ (Ruppert et al. 2006; Moriwaki and Kanda 2006); for a definition of similarity and dissimilarity between two scalars, see Dias and Brutsaert (1996).

Assumptions of perfect similarity are typically invoked within the extent of the atmospheric surface layer (ASL). In this region, under the validity of the assumptions of the Monin–Obukhov similarity theory (MOST), perfect

similarity (which is equivalent to perfect correlation between scalars) is guaranteed if the vertical turbulence transport of scalar variances and covariances is negligible (Dias and Brutsaert 1996). However, it is well known from field experiments that perfect similarity between scalars does not always hold in the ASL [e.g., see references in Katul et al. (2008) and Cancelli et al. (2012)]. Even though the physical process causing dissimilarity is not easily identifiable in field experiments, most authors tend to suggest a violation of one or more of the assumptions in MOST. Thus, nonstationarity (McNaughton and Laubach 1998; Asanuma et al. 2007), local advection (Asanuma et al. 2007), and surface heterogeneity (Andreas et al. 1998; Asanuma and Brutsaert 1999b; Lamaud and Irvine 2006) are usually suggested as causes for dissimilarity. Other potential candidates are the different active-passive roles of the scalars (Asanuma and Brutsaert 1999a,b; Katul and Parlange 1994) and possible effects of entrainment at the top of the ABL (de Bruin et al. 1993, 1999; Sempreviva and Gryning 2000; Asanuma et al. 2007).

Corresponding author address: Marcelo Chamecki, The Pennsylvania State University, 506 Walker Building, University Park, PA 16802.
E-mail: chamecki@psu.edu

Experimental data suggest that reduced similarity in the ASL is accompanied by scalar variance not following MOST—typically for the scalar that has the weakest surface forcing. This is the case for humidity over the land surface (Mahrt 1991; de Bruin et al. 1993; Roth and Oke 1995; Asanuma and Brutsaert 1999b; Katul and Hsieh 1999) and temperature over water surfaces (Semperviva and Gryning 1996; Cancelli et al. 2012). It is likely that weak surface forcing creates an opportunity for increased contributions from turbulence transport and possible effects of entrainment on ASL statistics. This observation led Cancelli et al. (2012) to formulate dimensionless criteria to diagnose similarity based on the strength of the surface fluxes.

It turns out that in practice it is very difficult to identify the cause for dissimilarity in field experiments because some degree of nonstationarity and surface heterogeneity is always present. However, in many cases these effects are small and not very likely to cause the large departures from perfect correlation observed between, say, temperature and specific humidity. For example, Cancelli et al. (2012) found that neither nonstationarity nor surface inhomogeneity could explain the high dissimilarity (different behavior of scalar fluctuations) found in many of their runs. Also, for homogeneous surfaces, de Bruin et al. (1993) and Li et al. (2012) found runs with low correlation coefficients. Therefore, entrainment fluxes or the active–passive roles of the scalars must play a role. Semperviva and Gryning (2000) emphasize the importance of entrainment fluxes on surface-layer dissimilarity and propose an ad hoc model for the correlation coefficient as a function of atmospheric stability and the height of the ABL.

If the attention is shifted to the region above the ASL, it is clear that in the upper part of the convective-mixed-layer temperature and specific humidity are anti-correlated (i.e., their covariance is negative yielding a negative bulk correlation coefficient) owing to the entrainment of warm dry air (Wyngaard et al. 1978; Katul et al. 2008). This effect is captured by the existing similarity models for the mixed layer, such as the top-down and bottom-up diffusion theory (Wyngaard and Brost 1984; Moeng and Wyngaard 1984) and the similarity theory of Sorbjan (1990, 1991), which yield vertical profiles of correlation coefficient that change from negative correlation at the top of the ABL to positive correlation near the surface. A number of numerical experiments using large-eddy simulation (LES) suggest that effects of entrainment fluxes can cause scalar dissimilarity even close to the surface (e.g., Sorbjan 2005, 2006; Lanotte and Mazzitelli 2013). In particular, Lanotte and Mazzitelli (2013) showed that increasing the strength of the inversion (which weakens the entrainment fluxes) increases

the correlation coefficients between temperature and a passive scalar throughout the entire ABL. However, no systematic investigation of the effects of entrainment fluxes on the surface layer has been performed, and direct evidence for these effects is still lacking (Asanuma et al. 2007). Katul et al. (2008) point out that the large distance separating the ASL and the entrainment zone and the ubiquitous presence of other possible sources of decorrelation make the argument for entrainment difficult to establish.

If the problem is approached from a mathematical perspective, dissimilarity can be caused by (i) differences in the prognostic equations for the scalars or (ii) different initial/boundary conditions. Therefore, if processes such as radiative effects or latent heating and the effects of the different molecular diffusivities are assumed to be negligible, the equations become identical and only the effects introduced through the initial/boundary conditions will influence the flow. Under these conditions, if one of the scalars is active and the other is passive, only the active scalar can modify the velocity field. However, both scalars will be transported and mixed exactly in the same way since they are both advected by the same velocity field. Therefore, passive–active properties cannot, by themselves, cause dissimilarity in a field that is initially perfectly similar. However, differences in active–passive roles may have the potential of greatly enhancing small dissimilarities present in the initial/boundary conditions and, in practice, may be very important (given that perfectly similar initial and boundary conditions are unlikely to exist). All other possible causes (nonstationarity, surface heterogeneity, local advection, and entrainment) must therefore be related to the boundary conditions. Asanuma and Brutsaert (1999b) suggest that nonstationarity should affect both scalars in the same way, but that is only true if the nonstationarity is originated from the velocity field or if it is equal in the boundary conditions for both scalars. Slightly different nonstationarity in the sensible and latent heat fluxes at the surface, as an example, would have different effects on temperature and specific humidity and could certainly lead to dissimilarity.

In this work we study the dissimilarity between temperature θ and specific humidity q in the ABL using an LES model. Idealized simulations are performed in which the choice of boundary conditions eliminates effects of heterogeneity and local advection. The focus is on the effects of entrainment fluxes on dissimilarity, emphasizing the mechanisms that lead to reduced correlation, the scales at which dissimilarity is found, and the resulting effects on scalar behavior within the ASL. In section 2 the numerical model and data analysis procedures are described. Results are

TABLE 1. LES domain size and grid resolution.

| Direction | x (downwind) | y (crosswind) | z (vertical) |
|-----------------|----------------|-----------------|----------------|
| Domain size (m) | 5120 | 5120 | 2048 |
| Grid points | 128 | 128 | 128 |
| Resolution (m) | 40 | 40 | 16 |

presented in section 3, and final discussions follow in section 4.

2. Numerical simulations

a. LES implementation and simulation setup

The LES model used in this work is described by Kumar et al. (2006), the only difference being the additional conservation equation for q . Specific humidity is treated as a passive scalar. The filtered Navier–Stokes and advection–diffusion equations are solved by a pseudospectral method in the horizontal directions and a second-order centered finite-difference formulation in the vertical direction. The model returns three-dimensional filtered fields for horizontal velocity wind components \tilde{u} and \tilde{v} , vertical wind velocity component \tilde{w} , and two scalars: temperature $\bar{\theta}$ and specific humidity \bar{q} . Prognostic equations for both scalars are identical. The dynamic Lagrangian scale-dependent subgrid-scale (SGS) model (Bou-Zeid et al. 2005) is used to close the momentum equations and constant SGS Prandtl and Schmidt numbers are used for temperature and specific humidity ($\text{Pr}_{\text{SGS}} = \text{Sc}_{\text{SGS}} = 0.4$ is assumed here).

Formally, any LES variable a can be written as $a = \tilde{a} + a_{\text{SGS}}$, where \tilde{a} and a_{SGS} are the resolved and subgrid-scale (or unresolved) components of a , respectively. The Reynolds decomposition can be applied to \tilde{a} , so $\tilde{a} = \bar{a} + \tilde{a}'$, where \bar{a} is the mean of the resolved part and \tilde{a}' is its fluctuation. In this work, statistics are calculated based on the resolved part and the tilde is omitted in order to simplify the notation. The second- and third-order moments that are analyzed here are typically dominated by contributions from the large scales in the turbulent flow. Therefore, except very close to the ground (and perhaps near the top of the ABL), we expect the contributions of the SGS components to be negligible and $\bar{a}'\bar{a}'$ to be a very good approximation to $\bar{a}'\bar{a}'$. The LES domain size and grid resolution used for all simulations are presented on Table 1.

To investigate the effects of the entrainment fluxes at the top of the ABL on scalar dissimilarity, we set up three simulations with the same initial temperature profile but distinct initial specific humidity profiles, as illustrated in Fig. 1. Case I—moistening in the mixed layer, drying above it—has the initial specific humidity

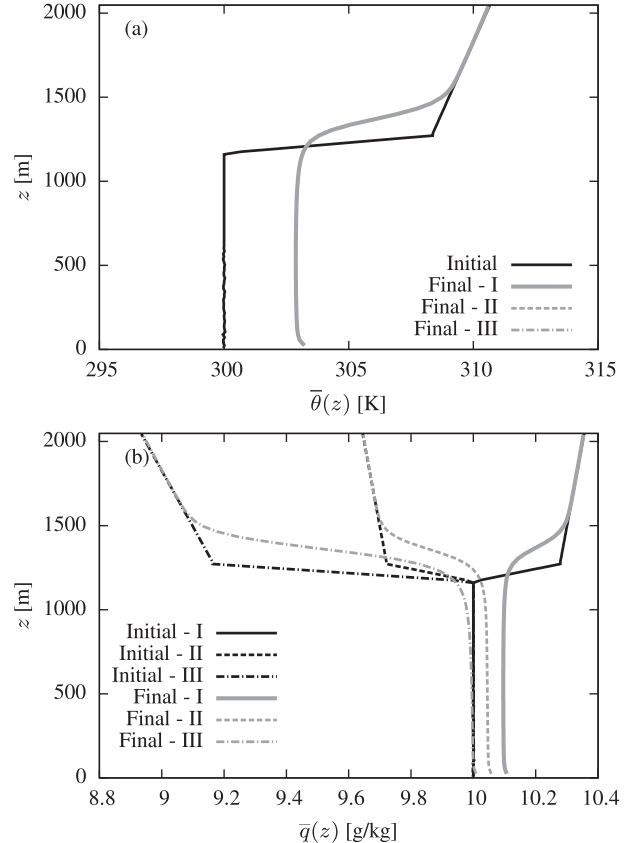


FIG. 1. Initial and final profiles of (a) mean temperature and (b) specific humidity for simulation cases I, II, and III.

profile q_0 increasing above z_i , following the behavior of the initial temperature profile θ_0 . This case is not intended to represent a physically relevant scenario for specific humidity, but rather to illustrate that if q and θ have identical initial and boundary conditions, the fact that one is active and the other is passive is not enough to cause dissimilarity in their time evolution. Case II has q_0 decreasing slowly with height above z_i , and is designed to represent the case of “moistening” of the ABL, in which the increase in specific humidity due to surface fluxes is larger than the drying due to entrainment fluxes (Sorbian 1990, 1991). Case III is similar to case II, except that the decrease in q_0 above z_i is much stronger, leading to very large entrainment fluxes and, consequently, a “drying” of the ABL. Both scalars are forced with constant positive surface fluxes at the ground. Therefore, in case I the boundary conditions for the two scalars are perfectly correlated at the top and bottom of the ABL, and perfect correlation is expected through the entire domain. Cases II and III are expected to generate perfect anticorrelation at the top of the domain, leading to dissimilarities between the two scalars within the ABL.

TABLE 2. Forcings used for the runs.

| Case | (u_g, v_g) (m s^{-1}) | $\overline{w'\theta'_0}$ ($\text{m s}^{-1} \text{K}$) | $\overline{w'q'_0}$ ($\text{m s}^{-1} \text{g kg}^{-1}$) |
|----------------|------------------------------------|---|--|
| I, II, and III | (1, 0) | 0.240 | 0.008 000 |
| IIa | (16, 0) | 0.240 | 0.008 000 |
| IIb | (16, 0) | 0.050 | 0.001 670 |
| IIc | (16, 0) | 0.025 | 0.000 833 |

In the three main simulations (cases I, II, and III—see Table 2) the velocity field is driven by a relatively small geostrophic wind (u_g, v_g) , while the surface sensible heat $(w'\theta'_0)$ and water vapor $(w'q'_0)$ fluxes are strong, thus producing a strongly convective ABL (i.e., as in free convection). During the simulations, the surface fluxes are kept constant (akin to midday conditions in a real boundary layer). To study scalar dissimilarity in the surface layer, three additional (less convective) simulations with the same initial profiles from case II are performed using a stronger geostrophic wind and progressively reducing surface heat and water vapor fluxes: they are called case IIa, case IIb, and case IIc, and the corresponding forcings are shown in Table 2. For all simulations, the initial z_i is set at 1167 m.

b. Data analysis

The simulation setup described in Tables 1 and 2 produces scalar fields that are not statistically stationary (in the sense that their means display a trend). The two possible approaches to avoid this issue are to calculate the desired statistics at one instant in time performing spatial averages (which requires larger horizontal domains than the ones used here) or to output time series of the desired fields at fixed locations and remove the unsteady component as typically done in analysis of experimental data. The second approach is used here. Time series of \tilde{u} , \tilde{w} , $\tilde{\theta}$, and \tilde{q} were output at an array of $16 \times 16 \times 64$ “virtual sensors” deployed respectively in the x , y , and z directions within the LES domain. These virtual sensors were equally spaced and data were recorded with a frequency of 0.2 Hz (the time step used in the simulations is 0.1 s, but only every fiftieth point was recorded to keep data outputs manageable and avoid recording redundant information as discussed below). This produced a total of 16 384 time series of 4 h for each simulation. Averages presented in this work are performed for the last 1.5 h of simulation.

Inspection of the time series suggests that the nonstationarity is dominated by a linear increase in temperature and specific humidity with time. A linear detrending was applied to each 1.5-h time series (for all output variables), and further inspection indicated that second- and third-order moments obtained from the

remaining fields are, to a very good approximation, statistically stationary. Statistics were calculated for each time series and then the vertical profiles were obtained by averaging in both horizontal directions. It should be noted that only half of the points, equally spaced, in the vertical (64 out of 128) are stored for postprocessing. Therefore, although the first simulation grid point is located at $z = 8$ m, the first vertical point of our profile is located at $z = 24$ m. To confirm that no effects of nonstationarity were present in the results, all profiles were also calculated based on horizontal averages within the LES domain followed by a 10-min average in time to improve statistical convergence. Results are nearly indistinguishable from the ones obtained from time series and presented in the next sections.

In addition to the vertical profiles, spectra, cospectra, and spectral correlation functions were estimated for each time series and then averaged over the horizontal array of 16×16 points, yielding one spectral function for each height. Note that the time step in the simulation is set to satisfy the Courant–Friedrichs–Lowy (CFL) condition at all heights, so the limitation on time resolution is set by $\Delta x/\tilde{u}$, which is typically much larger than Δt (and even more so closer to the surface where \tilde{u} becomes smaller). Close to the surface, even frequencies smaller than 0.2 Hz are damped by the spatial resolution. Therefore, only frequencies properly resolved are included in the spectral analysis.

Typical scales used to characterize turbulence in the mixed and surface layers and entrainment fluxes that are used in the next sections are presented in Table 3. For the surface-layer analysis in section 3c, u_* , θ_* , and q_* are the scales for velocity, temperature, and specific humidity, and are defined as

$$u_*^2 \equiv -\overline{u'w'_0}, \quad u_*\theta_* \equiv -\overline{w'\theta'_0}, \quad u_*q_* \equiv -\overline{w'q'_0}. \quad (1)$$

The subscript “0” indicates that the scales are based on the surface values of the constant fluxes (here calculated including the SGS contributions). Following Monin–Obukhov similarity theory, dimensionless turbulence statistics within the surface layer should be universal functions of the stability parameter z/Lo , where the Obukhov length Lo is defined by

$$Lo = \frac{-u_*^3 \bar{\theta}}{\kappa g w' \theta'_0}, \quad (2)$$

where $\kappa = 0.4$ is the Von Kármán constant, g is the gravitational acceleration, and $\bar{\theta}$ is the mean temperature at the first vertical grid point.

TABLE 3. Scaling parameters for each LES.

| Case | u_* (m s $^{-1}$) | θ_* (K) | q_* (g kg $^{-1}$) | Lo (m) | w_* (m s $^{-1}$) | Θ_* (K) | Q_* (g kg $^{-1}$) | z_i (m) | z_i/Lo | R_θ | R_q |
|------|----------------------|----------------|-----------------------|---------|----------------------|----------------|-----------------------|-----------|----------|------------|---------|
| I | 0.1106 | 2.1738 | 0.0725 | -0.94 | 2.1455 | 0.1119 | 0.0038 | 1272 | -1350.89 | -0.2117 | -0.2125 |
| II | 0.1106 | 2.1744 | 0.0725 | -0.98 | 2.1744 | 0.1119 | 0.0038 | 1272 | -1297.91 | -0.1505 | 0.5500 |
| III | 0.1069 | 2.2532 | 0.0751 | -0.85 | 2.1274 | 0.1128 | 0.0038 | 1240 | -1458.82 | -0.1667 | 2.1750 |
| IIa | 0.6013 | 0.4008 | 0.0134 | -140.76 | 2.1622 | 0.1110 | 0.0037 | 1304 | -9.26 | -0.2489 | 0.6287 |
| IIb | 0.4956 | 0.1024 | 0.0034 | -389.59 | 1.2523 | 0.0399 | 0.0013 | 1208 | -3.10 | -0.2752 | 0.5030 |
| IIc | 0.4816 | 0.0520 | 0.0018 | -736.92 | 0.9769 | 0.0256 | 0.0008 | 1144 | -1.55 | -0.4176 | 0.5965 |

For the convective mixed layer, the velocity scale is the convection velocity w_* (Deardorff 1970), and temperature and specific humidity scales must be obtained from w_* . Therefore, for the mixed-layer analysis presented in sections 3a and 3b, the scales are given by

$$w_* = \left(\frac{g}{\theta} \overline{w' \theta'_0 z_i} \right)^{1/3}, \quad w_* \Theta_* \equiv -\overline{w' \theta'_0}, \quad w_* Q_* \equiv -\overline{w' q'_0}, \quad (3)$$

where z_i is the atmospheric boundary layer height (which is determined as the minimum in the vertical heat flux profile). The ratio $-z_i/Lo$ is a bulk measure of the ABL instability and the parameters R_θ and R_q included in Table 3 are the ratios between fluxes of heat and water vapor at the top and the bottom of the ABL and enter the similarity theories for the mixed layer discussed in the next section (values of R_θ and R_q were estimated using only the resolved part of the vertical fluxes at the top of the ABL).

3. Results

a. Convective mixed layer

Vertical profiles of temperature and specific humidity variances, their covariance, and their correlation coefficient $r_{\theta q} = \overline{\theta' q'}/(\sigma_\theta \sigma_q)$ are presented in Fig. 2 for simulation cases I and II. As mentioned above, the only difference between these two simulations is the sign of the mean specific humidity gradient above the ABL (therefore, the sign of the specific humidity entrainment flux changes from being negative in case I to being positive in case II). In case I the initial profiles and boundary conditions for θ and q have the same shape and, as expected, the scalars are perfectly correlated within the entire ABL ($r_{\theta q} = 1$ in Fig. 2d), even though θ is active and q is passive. This result confirms the statement made in the introduction that, if the two scalars are perfectly correlated in the initial and boundary conditions, the active–passive distinction is not enough to decorrelate them.

The change of the sign of the specific humidity gradient above the ABL has a profound effect on the scalar

correlation, with $r_{\theta q}$ varying from +1.0 (perfectly correlated) at the ground to -1.0 (perfectly anticorrelated) close to the top of the ABL. Figures 2a and 2c show that the reduced correlation coefficient in case II is caused by a combination of the large increase in the specific humidity variance (Fig. 2b) and the change in the sign of the covariance $\overline{\theta' q'}$ at the top of the ABL (Fig. 2c). As expected, no changes are observed in the temperature variance shown in Fig. 2a (the boundary conditions for θ are exactly the same for cases I and II, and q is passive, so the velocity field is also the same). The correlation coefficient for case III is also shown in Fig. 2d, illustrating that results for the moistening ABL are also valid for the drying conditions. Similarly to Sorbjan (2005), the moistening case (II) has a larger correlation coefficient in the lower part of the ABL than the drying one (III).

To further investigate the contributions of these two changes to the scalar dissimilarity, vertical profiles of the ratios between statistics (variances and covariance) for case II by case I [e.g., $(\overline{\theta' \theta'})_{II}/(\overline{\theta' \theta'})_I$] and case III by case I are shown in Fig. 3. The figure suggests the existence of two distinct regions. Below $z/z_i \approx 0.5$, no significant deviations from 1 are observed in the temperature variance or the covariance term, indicating that the loss in correlation comes entirely from the increased variance of specific humidity. This additional variance in q must be a result of the entrainment of dry air at the top of the ABL. Note how the variance in q for cases II and III is increased compared to case I all the way down to the surface, being twice as large at the top of the ASL ($z/z_i \approx 0.2$) for case II and even larger for case III (the larger effect in case III is expected, based on the larger entrainment flux as seen in Table 3). Clearly this “extra variance” in specific humidity is completely decorrelated from temperature fluctuations below $z/z_i \approx 0.5$, as evidenced by the lack of changes in the covariance term. Above $z/z_i \approx 0.5$, the covariance term starts decreasing to change sign at $z/z_i \approx 0.7$. Therefore, above $z/z_i \approx 0.5$, both the reduction in the covariance and the increase in the variance of specific humidity contribute to the changes in the correlation coefficient.

The top-down and bottom-up diffusion theory (Wyngaard and Brost 1984; Moeng and Wyngaard 1984)

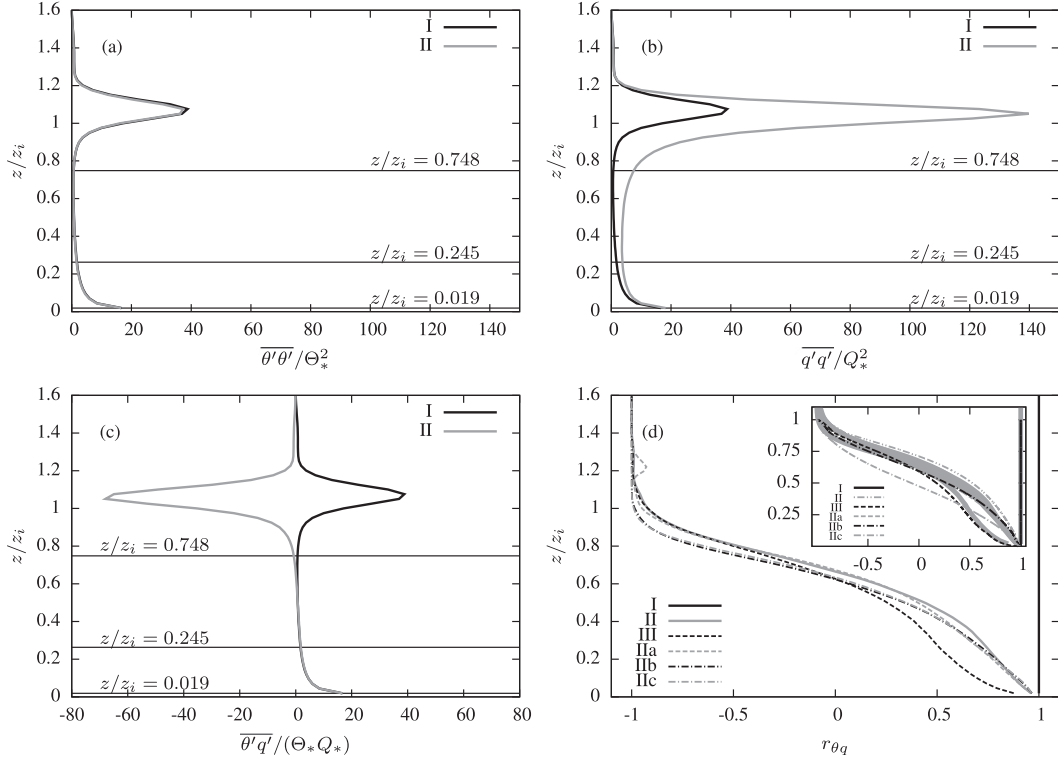


FIG. 2. Vertical profiles of (a) temperature variance, (b) specific humidity variance, (c) temperature–humidity covariance, and (d) correlation coefficient for simulation cases I and II. Additional simulations are also shown in (d), and the insert compares all the simulation results (gray curves) to the predictions of top-down and bottom-up diffusion theory.

yields equations for variances of temperature and humidity and their covariance (equations are presented in the appendix). The profiles for the correlation coefficient $r_{\theta q}$ obtained from the theory are shown in the insert in Fig. 2d. Note that the theory yields $r_{\theta q} = +1.0$ for case I, which is in perfect agreement with the LES results. For cases II and III, the theory captures the boundary conditions well (i.e., $r_{\theta q} = +1.0$ near the surface and $r_{\theta q} = -1.0$ near the top of the ABL), and it does a very good job within the entire ABL for all cases except case IIa (possibly related to the lower value of $-z_i/\text{Lo}$ for this run or to uncertainties in our estimates of R_θ and R_q , which do not include the subgrid-scale portion of the fluxes at the top of the ABL). The main implication of this good agreement between theory and LES results is that the mechanism causing the loss of correlation must be included in the theory, immediately eliminating nonstationarity as the main cause.

The physical mechanism causing the changes in the covariance term are quite obvious: if the gradients of temperature and specific humidity have different signs above the ABL, the entrained air for case II will have $\theta' > 0$ and $q' < 0$ (i.e., warmer and drier than the ABL air), causing the two scalars to be anticorrelated at $z/z_i \approx 1$.

However, the origin of the increase in the variance of q is less obvious. Inspection of Fig. 1 shows that in case I, as the ABL evolves, the differences in mean temperature and specific humidity between the ABL and the free atmosphere decrease. The opposite happens for specific humidity in case II: as the mean values of specific humidity increase inside the ABL owing to the evaporation

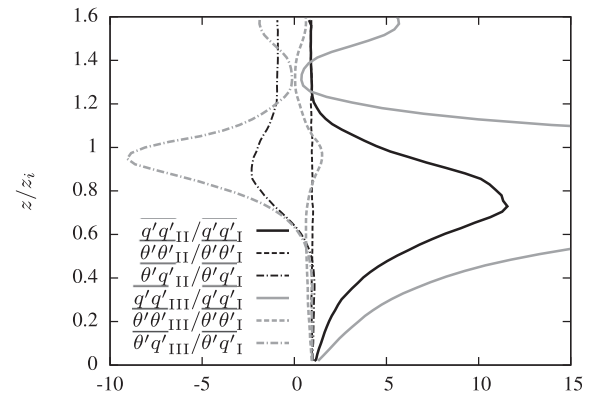


FIG. 3. Ratio between profiles of scalar variances of θ and q and their covariance (case II divided by case I and case III divided by case I).

at the surface, the contrast with the dry air above becomes larger, increasing the source of q variance due to entrainment. This large variance produced at the bottom of the entrainment region is then transported down through the entire ABL reaching the surface layer, as evidenced by Figs. 2b and 3. In order for this mechanism to be possible, turbulence transport of variance must exist within the entire ABL.

Further insight can be gained from the scalar variance budget. Assuming horizontal homogeneity, the budget equation for the variance of any scalar a is given by

$$\frac{\partial}{\partial t} \overline{a' a'} = P_a + T_a + S_a - \epsilon_a. \quad (4)$$

In Eq. (4), scalar variance production and dissipation are given by

$$P_{a'a'} = -2\overline{w' a' \frac{\partial \bar{a}}{\partial z}} \quad \text{and} \quad \epsilon_a = 2\nu_a \frac{\partial a' \partial a'}{\partial x_j \partial x_j}, \quad (5)$$

where ν_a is the scalar molecular diffusivity. The transport terms due to turbulence and subsidence are

$$T_a = -\frac{\partial}{\partial z} \overline{w' a' a'} \quad \text{and} \quad S_a = -\overline{w} \frac{\partial \overline{a' a'}}{\partial z}. \quad (6)$$

To estimate the transport terms for the specific humidity variance, simulations had to be extended for an additional 4 h (to improve statistical convergence of third-order moments) and the results presented in Fig. 4 represent averages over six simulation hours (processed in blocks of 1.5 h). Comparison of the mean variance profile from each block indicated that the transient term is very small (not shown) and a balance between the four terms on the right-hand side of Eq. (4) can be assumed. In case I, transport of specific humidity variance due to subsidence S_q is negligible within the entire ABL. Production P_q is positive everywhere except within $0.5 \leq z/z_i \leq 0.8$, where it is negative but fairly small (this indicates countergradient fluxes of specific humidity within this region, likely owing to the very large transport term). The turbulent transport term T_q is a source of variance throughout the entire ABL (except within the entrainment region) and it is the dominant term, confirming the highly nonlocal nature of $\overline{q' q'}$. In case II, the subsidence term now acts as a source of humidity variance below the entrainment zone. Both production and turbulent transport are increased when compared to case I. The main source of the additional variance in specific humidity in case II shown in Figs. 2b and 3 is now identified: the significant increase in production and vertical transport leads to much larger values of $\overline{q' q'}$

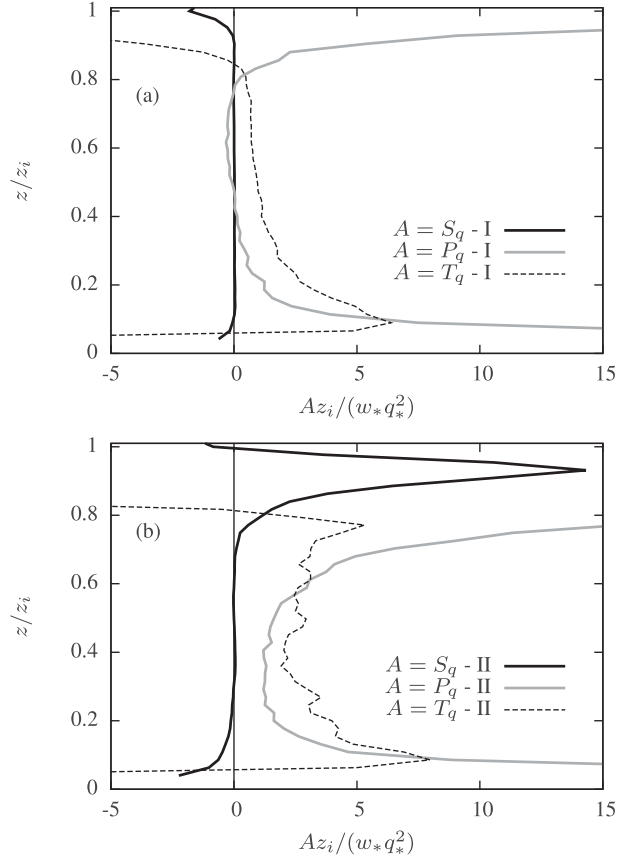


FIG. 4. Production and transport terms in the budget of specific humidity variance [Eq. (4)] for (a) case I and (b) case II. For both cases, the production and transport terms in the budget of the temperature variance are identical to the ones for specific humidity in case I.

throughout the entire ABL. This increase must be balanced by an equally important increase in the dissipation at the small scales.

Given the strong effect of vertical transport on the decorrelation of temperature and specific humidity in the lower portion of the ABL, one would expect air parcels in updrafts to be better correlated than the ones traveling in downdrafts (since the former would be more strongly affected by the surface fluxes while the latter would reflect the characteristics of entrained air). To verify that, variances and covariances are calculated conditioned on the value of the vertical velocity fluctuation [here, $w' > \sigma_w(z)$ is used as an identifier for updrafts and $w' < \sigma_w(z)$ for downdrafts]. The correlation coefficients for updrafts and downdrafts are compared to their counterparts for the entire dataset for cases II and III in Fig. 5. The fact that rising air parcels present much larger correlation coefficients than sinking ones provides further evidence of the large role played by entrainment and vertical transport on the decorrelation between scalars in the lower portion of the ABL.

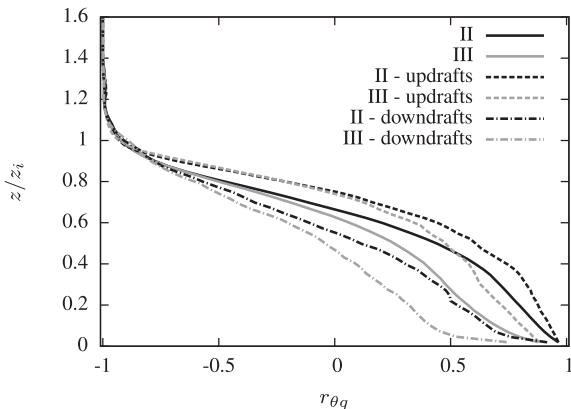


FIG. 5. Correlation coefficient between temperature and specific humidity for cases II and III sampled only in updrafts and downdrafts.

b. Spectral analysis

To determine the range of scales impacted by the entrainment effects described in the previous section, we estimated the (one sided) scalar spectra $S_{\theta\theta}(f)$ and $S_{qq}(f)$, the cospectrum between the two scalars $\text{Co}_{\theta q}(f)$, and the spectral correlation coefficient defined as

$$R_{\theta q}(f) = \frac{\text{Co}_{\theta q}(f)}{[S_{\theta\theta}(f)S_{qq}(f)]^{1/2}}, \quad (7)$$

where f is the frequency. These four spectral functions and the vertical velocity spectra $S_{ww}(f)$ are shown for three selected heights in Figs. 6a–e. The chosen heights illustrate spectral behavior near the surface ($z = 24$ m, $z/z_i \approx 0.019$), within the lower part of the mixed layer ($z = 312$ m, $z/z_i \approx 0.245$), and near the top of ABL ($z = 952$ m, $z/z_i \approx 0.748$)—these levels are also indicated by horizontal lines in Fig. 2. The temperature spectra for cases I and II are almost identical (Fig. 6c)—the small differences caused by run-to-run variation (two realizations of the same flow). Note that near the surface, the fast decay at the large frequency end is indicative that these frequencies cannot be fully resolved in the LES (this is a constraint imposed by the combination of grid resolution and advective velocity as discussed in section 2b) and that the resolution is just enough for the beginning of the inertial subrange to be captured.

Spectra for specific humidity are shown in Fig. 6d. Near the top of the ABL, the large increase in variance is distributed over the entire range of scales captured in the LES. This leads to larger levels of spectral variance flux within the inertial subrange and therefore larger values of dissipation of scalar variance, which is in agreement with the discussion of the balance presented in the

previous section. Within the lower portion of the mixed layer (at $z/z_i = 0.245$), most of the spectrum is still affected by the entrainment fluxes, except for the smallest resolved scales. However, close to the surface, only the very large scales are affected. The effects of entrainment observed near the surface are noticeable at frequencies smaller than 7×10^{-4} Hz, which correspond to time scales of about 24 min or longer, and could be interpreted as nonstationarity for the typical 30-min periods used in surface-layer data processing.

As expected, the cospectrum is only affected in the upper half of the domain (note that the cospectrum for case II at $z/z_i \approx 0.748$ is negative for $f < 0.02$ Hz and it is multiplied by -1 in the figure). The intriguing aspect here is the change in sign of the cospectrum at about $f = 0.02$ Hz. This is a fairly robust change so that all frequencies below this threshold have a negative cospectrum and all frequencies above it have a positive one, which is in agreement with measurements presented by Wyngaard et al. (1978). This effect is more clearly illustrated in Fig. 6f where the cospectra at several heights within the mixed layer are shown: while all the cospectra approximately collapse for case I, the gradual transition between an entirely positive and an entirely negative cospectrum happens first at the large scale and moves toward smaller scales as z/z_i increases. The cospectra for case II cannot fit the traditional picture of a single cascade of covariance from large to small scales, and is likely to be indicative of different processes governing the cospectrum at different scales. The small scales are probably dominated by locally produced positive covariance and the large scales dominated by nonlocal covariance being transported from the entrainment zone.

Finally, the analysis of $R_{\theta q}$ shown in Fig. 6e is very revealing. For case I, $R_{\theta q} = 1$ at all scales at all heights. For case II, a few interesting observations can be made: 1) close to the surface the smaller scales are highly correlated while the correlation is weaker but significant (about 0.8) in the larger scales; 2) farther away from the surface, the correlation becomes weaker at the large scales and the small scales are no longer perfectly correlated (there is a gradual loss of correlation across the spectrum, but the smaller scales are always more correlated than the larger ones); and 3) closer to the top of the ABL, where the bulk correlation coefficient is negative, the small scales still have a very weak positive correlation while the larger scales become strongly anticorrelated. Therefore, closer to the surface, most of the (positive) correlation captured in $r_{\theta q}$ comes from the smaller scales, while closer to the top of the ABL most of the (negative) correlation captured by $r_{\theta q}$ comes from the larger scales—a very interesting asymmetry.

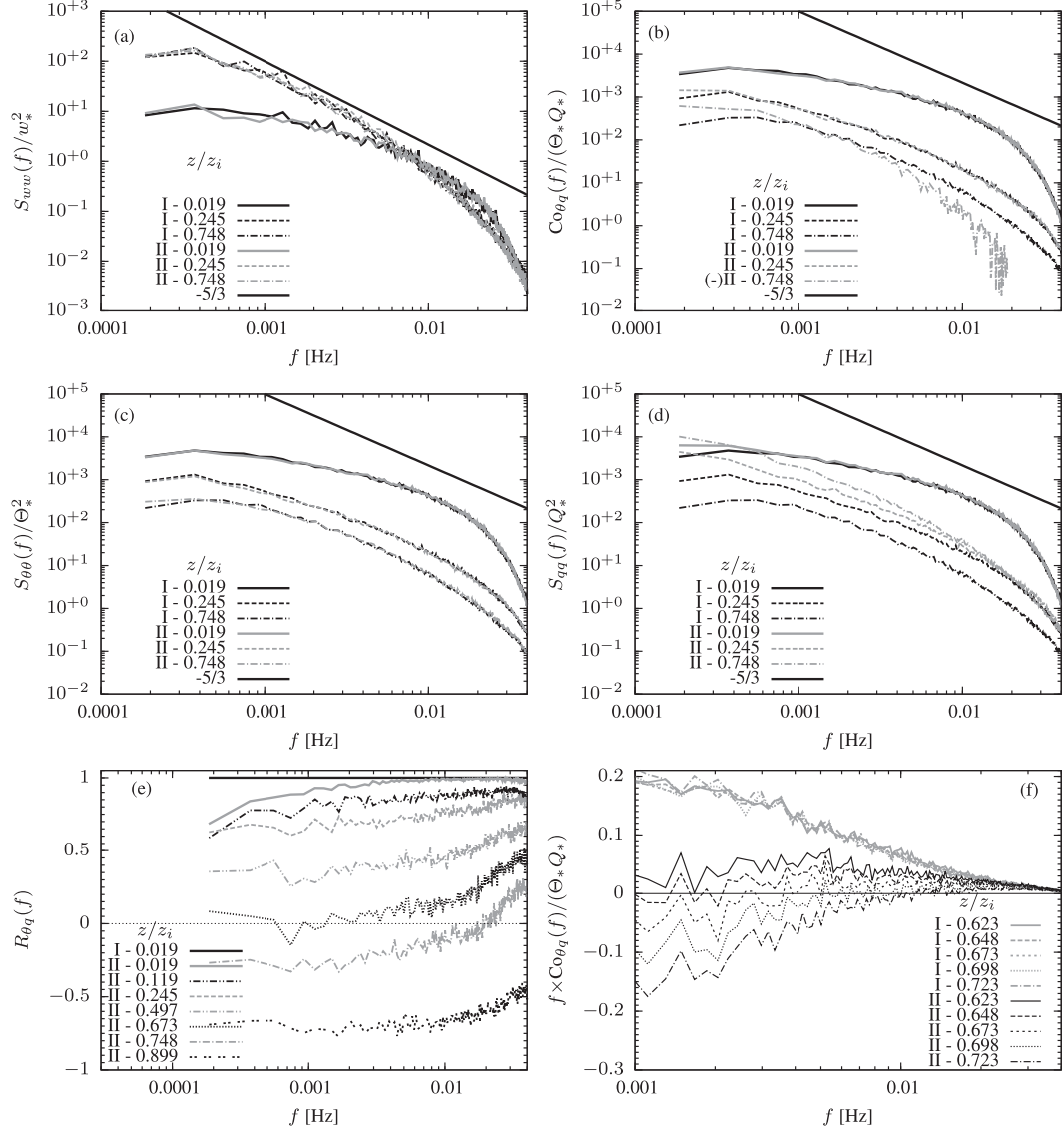


FIG. 6. Spectral analysis for simulation cases I and II at selected heights. (a) Vertical velocity spectra, (b) temperature–humidity cospectra, (c) temperature spectra, (d) specific humidity spectra, (e) spectral correlation coefficient, and (f) frequency premultiplied temperature–humidity cospectra. Note that the cospectra at $z/z_i = 0.748$ is multiplied by a factor -1 in (b) and all the spectral correlation coefficients for case I collapse at $+1$ in (e).

c. Effects on surface-layer turbulence

As mentioned in section 2a, in order to study the effects of entrainment at the top of the ABL on surface-layer scalar dissimilarity, a set of three additional (less convective) simulations were performed (see Table 2). The relevant scales and parameters are listed in Table 3 and $r_{\theta q}$ is presented in Fig. 2d. It is interesting to note the collapse of the correlation coefficient for the different simulations when plotted against z/z_i , suggesting that the shape of the curve presented in Fig. 2d is independent of z_i/Lo for the range investigated here (note the

very large range of z_i/Lo in Table 3). For the purpose of the present ASL analysis, only points that simultaneously satisfy the conditions $z/z_i < 0.2$ and $|z/\text{Lo}| < 2$ are considered.

Figure 7a shows the standard deviation of θ and q against z/Lo together with the universal function of MOST for unstable conditions given by (Kaimal and Finnigan 1994):

$$\frac{\sigma_\theta}{\theta_*} \frac{\sigma_q}{q_*} = 2(1 + 9.5|z/\text{Lo}|)^{-1/3}. \quad (8)$$

The agreement between data from the three simulations is better for σ_q/q_* than for σ_θ/θ_* . In addition, the behavior

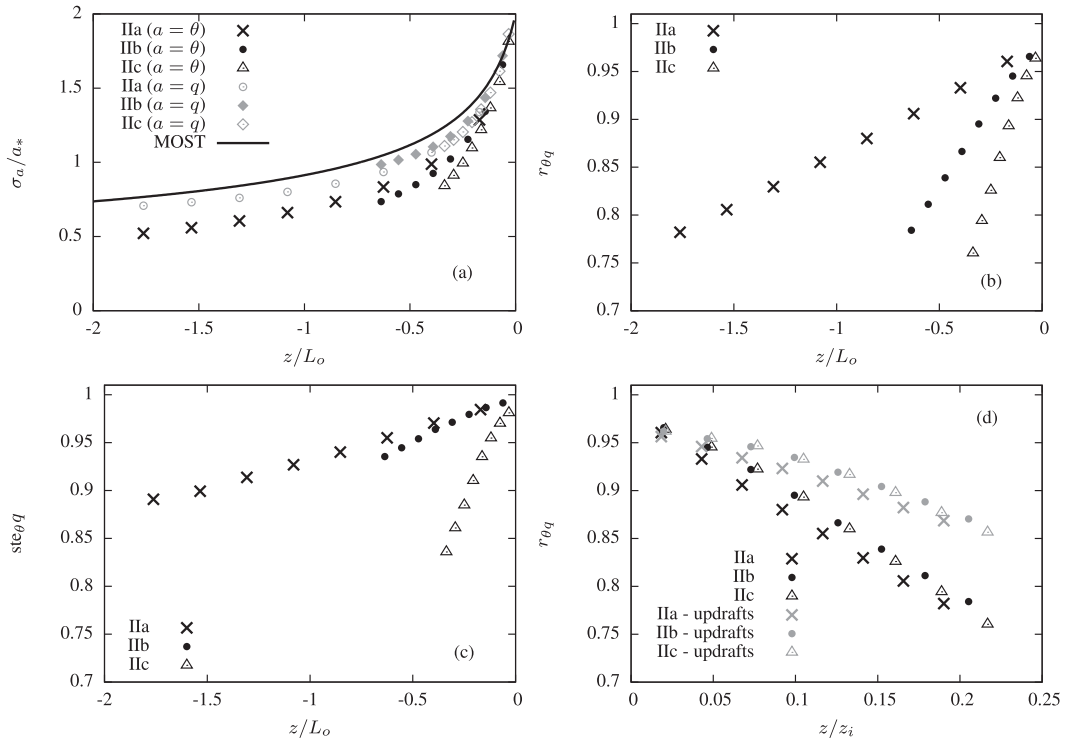


FIG. 7. Surface-layer analysis for simulation cases IIa, IIb, and IIc. Temperature and specific humidity (a) standard deviation, (b) correlation coefficient, and (c) symmetric transfer efficiency. (d) The correlation coefficient is also shown using mixed-layer scaling.

of the two scalars is clearly different, with σ_q/q_* being closer to Eq. (8). Similar behavior is observed for the normalized covariance $\overline{\theta'q'}/(\theta_*q_*)$ (not shown). These small differences result in correlation coefficients significantly smaller than 1 within the surface layer, as illustrated in Fig. 7b. It could be noted that as the surface fluxes become weaker the correlation decays faster with z/Lo , clearly indicating that weakening the surface forcing leads to a stronger effect of the entrainment fluxes (top-down diffusion). Perhaps more importantly, the curves for the different simulations do not collapse when plotted against z/Lo . This is to be expected: $|r_{\theta q}| < 1$ represents deviations from MOST due to contributions from the entrainment fluxes, and there is no reason to expect that these deviations should scale with MOST parameter z/Lo . The collapse of $r_{\theta q}$ as a function of z/z_i obtained in Fig. 2d may suggest a complete independence of Lo . The surface-layer points are shown again in Fig. 7d, this time displayed against z/z_i . The collapse of the three simulations is much better than the one obtained against z/Lo . Note also that if the statistics are sampled only in updrafts [defined as points where $w' > \sigma_w(z)$, as done in section 3a], correlation coefficients are significantly larger (gray symbols in Fig. 7d) suggesting that entrainment fluxes are also responsible for decorrelation within the surface layer.

The effect of entrainment fluxes on scalar dissimilarity within the surface layer can be further studied by inspecting the spectral correlation coefficients shown in Fig. 8. The panels corresponding to cases IIa and IIc are quite similar to each other, further indicating the independence of the dissimilarity on z/Lo . Closer to the surface, $R_{\theta q}$ is approximately +1 at the high frequencies, and the dissimilarity is contained within the low-frequency range. Farther from the surface, a loss of correlation across the spectrum is observed. The most interesting feature of Fig. 8 is perhaps the strong dip in $R_{\theta q}$ observed at frequencies comparable to the inverse of the eddy turnover time scale for mixed layer eddies given by $f = w_*/z_i$. This prominent feature has been observed in experimental data reported by Asanuma et al. (2007) and Cancelli et al. (2012) and confirms once again the role of mixed-layer eddies on surface-layer dissimilarity. It is not clear why the simulation case II does not have this strong dip in $R_{\theta q}$ (Fig. 6d).

Noting that near the surface most of the dissimilarity is contained in the low frequencies, it is of interest to investigate if similarity can be recovered by filtering out the low-frequency components of θ and q . The peak of the premultiplied vertical velocity spectrum [i.e., $fS_{ww}(f)$] is used to determine the frequency for the spectral cutoff filter. The peak is determined by fitting the function $fS_{ww}(f)/u_*^2 = An[1 + (Bn)^{5/3}]^{-1}$ to the spectrum of vertical

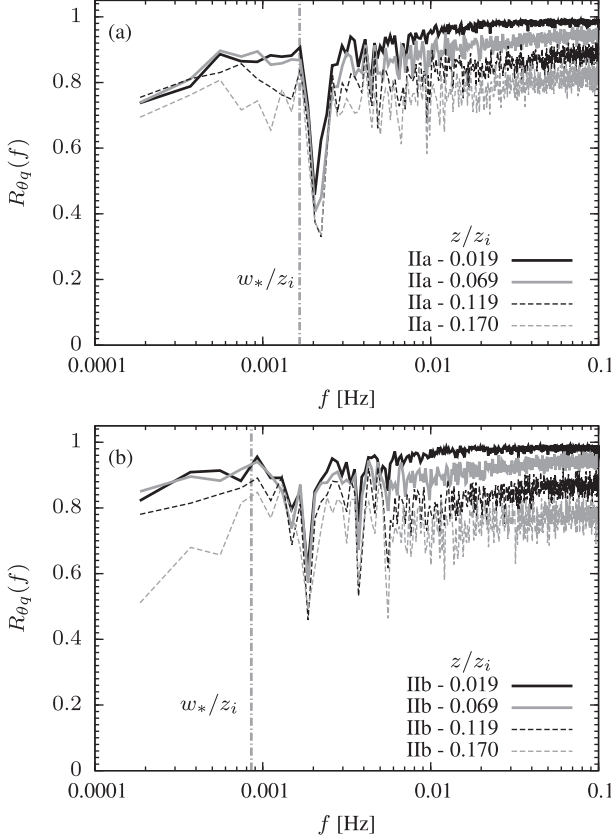


FIG. 8. Spectral correlation coefficient at several heights within the surface layer for simulations (a) IIa and (b) IIc. The vertical line corresponds to the frequency of mixed-layer eddies w_*/z_i .

velocity (Kaimal et al. 1972) at each level z (here $n = fz/\bar{u}$ is the normalized frequency, and A and B are constants adjusted for the function to fit the LES data). The cutoff frequency is $f_c = n_0\bar{u}/z$, where n_0 is the normalized frequency corresponding to the peak in $An[1 + (Bn)^{5/3}]^{-1}$. The correlation coefficients for the filtered data are compared to the original ones in Fig. 9. A significant gain in correlation is observed, and the correlation coefficient close to the surface becomes very close to +1.

Finally, several methods of practical importance to estimate scalar fluxes rely on the similarity between the vertical fluxes of scalars, which is less sensitive to scalar dissimilarity than $r_{\theta q}$ (Cancelli et al. 2012). The similarity between the fluxes can be quantified by the symmetric transfer efficiency introduced by Cancelli et al. (2012) and defined as

$$\text{ste}_{\theta q} = 1 - \frac{\|r_{w\theta} - r_{wq}\|}{\|r_{w\theta} + r_{wq}\|}. \quad (9)$$

Note that this is a better indicator than the usually employed relative transfer efficiency ($\text{ rte}_{\theta q} = r_{w\theta}/r_{wq}$)

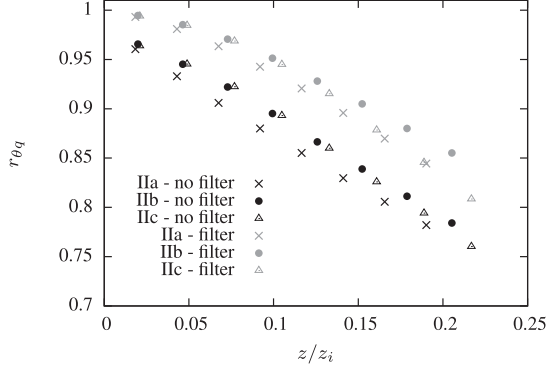


FIG. 9. Correlation coefficient between temperature and specific humidity for cases IIa, IIb, and IIc before and after applications of high-pass filter.

for being symmetrical in θ and q and bounded by 1. In Fig. 7c we present the $\text{ste}_{\theta q}$ within the surface layer. Comparison with the values for $r_{\theta q}$ confirms that the scalar transfer is more similar than the scalars themselves, supporting the applicability of methods based on transfer efficiency similarity.

4. Discussion

Simulation results presented here clearly show that in the lower half of the ABL, loss of correlation can be caused by entrainment fluxes through an increase in scalar variance. In the present case, this increase was associated with specific humidity, but it is possible that different boundary conditions would lead to an increase in temperature variance as well. This increased variance results from enhancement in the local production term and in the (nonlocal) vertical turbulent transport of variance from above. The nonlocal effects on the variance cause departures from MOST, which is consistent with experimental results (Mahrt 1991; de Bruin et al. 1993; Roth and Oke 1995; Asanuma and Brutsaert 1999b; Katul and Hsieh 1999; Sempreviva and Gryning 1996). These results provide further support to the criteria presented by Cancelli et al. (2012): in cases of stronger surface forcing, local production and dissipation dominate the balance and entrainment effects should become less important within the ASL, leading to higher correlation between scalars.

Spectral analysis shows that although the increases in variance occur at all scales within the convective mixed layer, only the very large scales seem to be affected in the lower part of the ASL. A number of experimental studies report nonstationarity and low-frequency dissimilarity as being responsible for lower correlation coefficients within the ASL (McNaughton and Laubach 1998; Dias et al. 2004; Asanuma et al. 2007; Cancelli et al.

2012). The present work suggests that the entrainment fluxes could be the cause behind these large-scale effects.

Clearly, the effects of turbulence transport within the ASL must be reduced as the value of $-z_i/\text{Lo}$ is reduced and the simulation becomes less convective. However, the decay of $r_{\theta q}$ with z/z_i remains unchanged for the portion of the parameter space explored here. Further research is needed to confirm the collapse of $r_{\theta q}$ against z/z_i observed in Fig. 7d. Sempreviva and Gryning (2000) studied the effects of entrainment on similarity and proposed a model $r_{\theta q} = 0.9/(1 - 2\text{Lo}/z_i)$. These authors suggest that a better model should incorporate R_θ and R_q . If the results obtained here are confirmed for different conditions, perhaps Lo plays a minimal role in the dissimilarity, and the top-down and bottom-up diffusion theory may actually be used to estimate the correlation coefficient even within the ASL. In any case, the lack of collapse of $r_{\theta q}$ against z/Lo seems to be a robust result when the dissimilarity is caused by entrainment fluxes. Obviously, other causes for dissimilarity exist, and similar numerical simulations could be used to quantify effects of surface heterogeneity. However, results presented here suggest that in the absence of other obvious sources of dissimilarity (such as surface heterogeneity or nonstationarity of surface fluxes), entrainment should be considered the main possible cause of dissimilarity observed in experimental data.

Last, it is reasonable to expect that the effects of entrainment on the surface layer extend beyond scalar variances and covariances. As noted by Kanda et al. (2004), sensible and latent heat fluxes within the ASL may also be affected by entrainment and the structure of the convective boundary layer. Salesky and Chamecki (2012) suggested that deviations from MOST in experimental data may also be correlated to the height of the ABL. Therefore, the effects of entrainment and large-scale ABL processes on the surface fluxes and other ASL quantities might be important. However, more research will be needed to clarify this issue.

Acknowledgments. This research was performed while DMC was a visiting student at the Department of Meteorology at The Pennsylvania State University with support from the Brazilian Science Without Borders program through CNPq/MCT (Process 201974/2011-8).

APPENDIX

Predictions from Top-Down and Bottom-Up Diffusion Theory

Moeng and Wyngaard (1984) proposed a top-down and bottom-up diffusion theory that yields equations for

variances of temperature and humidity and their covariance. These dimensionless theoretical functions are

$$\frac{\overline{\theta' \theta'}}{\Theta_*^2} = f_b + 2R_\theta f_{tb} + R_\theta^2 f_t, \quad (\text{A1})$$

$$\frac{\overline{q' q'}}{\Theta_*^2 Q_*} = f_b + 2R_q f_{tb} + R_q^2 f_t, \quad \text{and} \quad (\text{A2})$$

$$\frac{\overline{\theta' q'}}{\Theta_* Q_*} = f_b + (R_\theta + R_q)f_{tb} - R_\theta R_q f_b. \quad (\text{A3})$$

Here, R_θ and R_q are the ratios between fluxes of heat and water vapor at the top and the bottom of the CBL, and f_b , f_t , and f_{tb} are given by

$$f_b = \begin{cases} 1.8(z/z_i)^{-2/3} & \text{for } z/z_i < 0.1z_i \\ 0.47(z/z_i)^{-5/4} & \text{for } z/z_i > 0.1z_i \end{cases}, \quad (\text{A4})$$

$$f_t = \begin{cases} 2.1(1-z/z_i)^{-3/2} & \text{for } z/z_i < 0.9z_i \\ 14(1-z/z_i)^{-2/3} & \text{for } z/z_i > 0.9z_i \end{cases}, \quad \text{and} \quad (\text{A5})$$

$$f_{tb} = 1, \quad (\text{A6})$$

where z_i is the boundary layer height. Note that all the coefficients were obtained by Moeng and Wyngaard (1984) using an LES code similar to the ones used here, and therefore it is no surprise that there is very good agreement between the theoretical profiles and the numerical results presented in this work.

REFERENCES

- Andreas, E. L., R. J. Hill, J. R. Gosz, D. I. Moore, W. D. Otto, and A. D. Sarma, 1998: Stability dependence of the eddy-accumulation coefficients for momentum and scalars. *Bound.-Layer Meteor.*, **86**, 409–420.
- Asanuma, J., and W. Brutsaert, 1999a: The effect of chessboard variability of the surface fluxes on the aggregated turbulence fields in a convective atmospheric surface layer. *Bound.-Layer Meteor.*, **91**, 37–50.
- , and —, 1999b: Turbulence variance characteristics of temperature and humidity in the unstable atmospheric surface layer above a variable pine forest. *Water Resour. Res.*, **35**, 515–521.
- , H. Ishikawa, I. Tamagawa, Y. Ma, T. Hayashi, Y. Qi, and J. Wang, 2005: Application of the band-pass covariance technique to portable flux measurements over the Tibetan Plateau. *Water Resour. Res.*, **41**, W09407, doi:10.1029/2005WR003954.
- , I. Tamagawa, H. Ishikawa, Y. Ma, T. Hayashi, Y. Qi, and J. Wang, 2007: Spectral similarity between scalars at very low frequencies in the unstable atmospheric surface layer over the Tibetan Plateau. *Bound.-Layer Meteor.*, **122**, 85–103.

- Bou-Zeid, E., C. Meneveau, and M. B. Parlange, 2005: A scale-dependent Lagrangian dynamic model for large-eddy simulation of complex turbulent flows. *Phys. Fluids*, **17**, 025105, doi:10.1063/1.1839152.
- Cancelli, D. M., N. L. Dias, and M. Chamecki, 2012: Dimensionless criteria for the production-dissipation equilibrium of scalar fluctuations and their implications for scalar similarity. *Water Resour. Res.*, **48**, W10522, doi:10.1029/2012WR012127.
- Deardorff, J. W., 1970: Convective velocity and temperature scales for the unstable planetary boundary layer and for Rayleigh convection. *J. Atmos. Sci.*, **27**, 1211–1212.
- de Bruin, H. A. R., W. Kohsiek, and B. J. J. M. van der Hurk, 1993: A verification of some methods to determine the fluxes of momentum, sensible heat, and water vapor using standard deviation and structure parameter of scalar meteorological quantities. *Bound.-Layer Meteor.*, **63**, 231–257.
- , B. J. J. M. van den Hurk, and L. J. M. Kroon, 1999: On the temperature-humidity correlation and similarity. *Bound.-Layer Meteor.*, **93**, 453–468.
- Dias, N. L., and W. Brutsaert, 1996: Similarity of scalars under stable conditions. *Bound.-Layer Meteor.*, **80**, 355–373.
- , M. Chamecki, A. Kan, and C. M. P. Okawa, 2004: A study of spectra, structure and correlation functions and their implication on the stationarity of surface-layer turbulence. *Bound.-Layer Meteor.*, **110**, 165–189.
- Kaimal, J. C., and J. J. Finnigan, 1994: *Atmospheric Boundary Layer Flows: Their Structure and Measurement*. Oxford University Press, 289 pp.
- , J. C. Wyngaard, Y. Izumi, and O. R. Coté, 1972: Spectral characteristics of surface layer turbulence. *Quart. J. Roy. Meteor. Soc.*, **98**, 563–589.
- Kanda, M., A. Inagaki, M. Letzel, S. Raasch, and T. Watanabe, 2004: LES study of the energy imbalance problem with eddy covariance fluxes. *Bound.-Layer Meteor.*, **110**, 381–404.
- Katul, G. G., and M. B. Parlange, 1994: On the active role of temperature in surface-layer turbulence. *J. Atmos. Sci.*, **51**, 2181–2195.
- , and C.-I. Hsieh, 1999: A note on the flux-variance similarity relationships for heat and water vapour in the unstable atmospheric surface layer. *Bound.-Layer Meteor.*, **90**, 327–338.
- , A. M. Sempreviva, and D. Cava, 2008: The temperature-humidity covariance in the marine surface layer: A one-dimensional analytical model. *Bound.-Layer Meteor.*, **126**, 263–278, doi:10.1007/s10546-007-9236-z.
- Kumar, V., J. Kleissl, C. Meneveau, and M. B. Parlange, 2006: Large-eddy simulation of a diurnal cycle of the atmospheric boundary layer: Atmospheric stability and scaling issues. *Water Resour. Res.*, **42**, W06D09, doi:10.1029/2005WR004651.
- Lamaud, E., and M. Irvine, 2006: Temperature-humidity dissimilarity and heat-to-water-vapour transport efficiency above and within a pine forest canopy: The role of the Bowen ratio. *Bound.-Layer Meteor.*, **120**, 87–109.
- Lanotte, A., and I. M. Mazzitelli, 2013: Scalar turbulence in convective boundary layers by changing the entrainment flux. *J. Atmos. Sci.*, **70**, 248–265.
- Li, D., E. Bou-Zeid, and H. A. R. De Bruin, 2012: Monin–Obukhov similarity functions for the structure parameters of temperature and humidity. *Bound.-Layer Meteor.*, **145**, 45–67, doi:10.1007/s10546-011-9660-y.
- Mahrt, L., 1991: Boundary-layer moisture regimes. *Quart. J. Roy. Meteor. Soc.*, **117**, 151–176.
- McNaughton, K. G., and J. Laubach, 1998: Unsteadiness as a cause of non-equality of eddy diffusivities for heat and vapour at the base of an advective inversion. *Bound.-Layer Meteor.*, **88**, 479–504.
- Moeng, C.-H., and J. C. Wyngaard, 1984: Statistics of conservative scalars in the convective boundary layer. *J. Atmos. Sci.*, **41**, 3161–3169.
- Moriwaki, R., and M. Kanda, 2006: Local and global similarity in turbulent transfer of heat, water vapor, and CO₂ in the dynamic convective sublayer over a suburban area. *Bound.-Layer Meteor.*, **120**, 163–179.
- Roth, M., and T. Oke, 1995: Relative efficiencies of turbulent transfer of heat, mass, and momentum over a patchy urban surface. *J. Atmos. Sci.*, **52**, 1863–1874.
- Ruppert, J., C. Thomas, and T. Foken, 2006: Scalar similarity for relaxed eddy accumulation methods. *Bound.-Layer Meteor.*, **120**, 39–63.
- Salesky, S., and M. Chamecki, 2012: Random errors in turbulence measurements in the atmospheric surface layer: Implications for Monin–Obukhov similarity theory. *J. Atmos. Sci.*, **69**, 3700–3714.
- Semperviva, A. M., and S.-E. Gryning, 1996: Humidity fluctuations in the marine boundary layer measured at a coastal site with an infrared humidity sensor. *Bound.-Layer Meteor.*, **77** (3–4), 331–352.
- , and —, 2000: Mixing height over water and its role on the correlation between temperature and humidity fluctuations in the unstable surface layer. *Bound.-Layer Meteor.*, **97**, 273–291.
- Sorbian, Z., 1990: Similarity scales and universal profiles of statistical moments in the convective boundary layer. *J. Appl. Meteor.*, **29**, 762–775.
- , 1991: Evaluation of local similarity functions in the convective boundary layer. *J. Appl. Meteor.*, **30**, 1565–1583.
- , 2005: Statistics of scalar fields in the atmospheric boundary layer based on large-eddy simulations. Part 1: Free convection. *Bound.-Layer Meteor.*, **116**, 467–486.
- , 2006: Statistics of scalar fields in the atmospheric boundary layer based on large-eddy simulations. Part 2: Forced convection. *Bound.-Layer Meteor.*, **119**, 57–79.
- Wesely, M. L., 1988: Use of variance techniques to measure dry air-surface exchange rates. *Bound.-Layer Meteor.*, **44**, 13–31.
- Wyngaard, J. C., and R. A. Brost, 1984: Top-down and bottom-up diffusion of a scalar in the convective boundary layer. *J. Atmos. Sci.*, **41**, 102–112.
- , W. T. Pennell, D. H. Lenschow, and M. A. Lemone, 1978: The temperature-humidity covariance budget in the convective boundary layer. *J. Atmos. Sci.*, **35**, 47–58.